Noname manuscript No.
(will be inserted by the editor)

NIRS3: The Near Infrared Spectrometer on Hayabusa2

Takahiro Iwata · Kohei Kitazato · Masanao Abe · Makiko Ohtake · Takehiko Arai · Tomoko Arai · Naru Hirata · Takahiro Hiroi · Chikatoshi Honda · Naoya Imae · Mutsumi Komatsu · Tsuneo Matsunaga · Moe Matsuoka · Shuji Matsuura · Tomoki Nakamura · Aiko Nakato · Yusuke Nakauchi · Takahito Osawa · Hiroki Senshu · Yasuhiko Takagi · Kohji Tsumura · Naruhisa Takato · Sei-ichiro Watanabe · Maria Antonietta Barucci · Ernesto Palomba · Masanobu Ozaki

Received: date / Accepted: date

T. Iwata • M. Abe • M. Ohtake • Y. Nakauchi • M. Ozaki
Institute of Space and Astronautical Science, Japan Aerospace Exploration Agency
Sagamihara Campus, SOKENDAI
3-1-1 Yoshinodai, Chuo-ku, Sagamihara, Kanagawa, 252-5210, Japan,
Tel.: +81-50-3362-3618
Fax: +81-42-759-8510
E-mail: iwata.takahiro@jaxa.jp

K. Kitazato • N. Hirata • C. Honda
The University of Aizu, Aizuwakamatsu, Japan

Takehiko Arai • T. Matsunaga
National Institute for Environmental Studies, Tsukuba, Japan

Tomoko Arai • H. Senshu
Chiba Institute of Technology, Narashino, Japan

T. Hiroi
Brown University, Providence, USA

N. Imae
National Institute of Polar Research, Tachikawa, Japan

M. Komatsu
SOKENDAI, Hayama-machi, Japan

M. Matsuoka • T. Nakamura • K. Tsumura
Tohoku University, Sendai, Japan

S. Matsuura
Kwansei Gakuin University, Sanda, Japan

A. Nakato
Kyoto University, Kyoto, Japan

T. Osawa
Japan Atomic Energy Agency, Tokai-mura, Japan

Y. Takagi
Aichi Toho University, Nagoya, Japan

N. Takato
Subaru Telescope, National Astronomical Observatory of Japan, Hilo, USA

S. Watanabe
Nagoya University, Nagoya, Japan

M. A. Barucci
LESIA Observatorie de Paris, Centre National d'Études Spatiales, Meudon, France

E. Palomba
INAF, Instituto di Astrofisica e Planetologia Spaziali, Rome, Italy

Abstract NIRS3: The Near Infrared Spectrometer is installed on the Hayabusa2 spacecraft to observe the target C-type asteroid 162173 Ryugu at near infrared wavelengths of 1.8 to 3.2 μm. It aims to obtain reflectance spectra in order to detect absorption bands of hydrated and hydroxide minerals in the 3μm-band. We adopted a linear-image sensor with indium arsenide (InAs) photo diodes and a cooling system with a passive radiator to achieve an optics temperature of 188 K (-85°C), which enables to retaining sufficient sensitivity and noise level in the 3-μm wavelength region. We conducted ground performance tests for the NIRS3 flight model (FM) to confirm its baseline specifications. The results imply that the properties such as the signal-to-noise ratio (SNR) conform to scientific requirements to determine the degree of aqueous alteration, such as CM or CI chondrite, and the stage of thermal metamorphism on the asteroid surface.

Keywords Hayabusa2 · NIRS3 · Asteroid · Near Infrared · Spectrometer

1 Introduction

The Hayabusa2 spacecraft, which was successfully injected into a cruising orbit toward the target asteroid 162173 Ryugu (1999 JU3) on December 3, 2014, seeks to explore a primitive asteroid to understand the origin and evolution of solar system materials such as water and organic matters. The spacecraft is scheduled to arrive at Ryugu in 2018 and then execute remote sensing observations for more than one year. Asteroid Ryugu is categorized as a C-type asteroid based on its extended visible reflectance spectra (Binzel et al. 2001; Lazzaro et al. 2013) and is implied to have surface heterogeneity in the degrees of aqueous alteration from ground-based observations (Vilas 2008). The geometric albedo is estimated as 0.070±0.006, and the surface temperature on the dayside is about 300 K (Müller et al. 2010). It is believed to have suffered orbital degradation from a main-belt asteroid to a near-earth asteroid (Campins et al. 2013). The current orbit of Ryugu is close enough to that of the Earth and approachable by a spacecraft within the launch capacity of the H-IIA launch vehicle. Therefore, Ryugu is a unique C-type asteroid to which a sample-return mission can be realized.

The Near Infrared Spectrometer NIRS3 onboard the Hayabusa2 spacecraft will perform near-infrared spectroscopy for wavelengths from 1.8 to 3.2 μm with sensitivity for molecular absorption by hydroxide and hydrated minerals at 2.7 to 3.0 μm. The design of NIRS3 follows the heritage of NIRS that was on Hayabusa and performed successful spectroscopy in the 0.76 to 2.1 μm wavelength region (Abe et al. 2006). To extend the wavelength to the 3 μm band, we adopted a new linear-image sensor and a cooling system that do not need active coolers. We conducted ground performance tests and calibration tests for the NIRS3 flight model (FM) before and after environmental tests from July 2013 to May 2014. We examined whether the performance satisfies requirements by using the test results. We also observed reflected spectra of minerals, C chondrites (Nakamura et al. 2015), and calibration plates of MicrOmega (Bibring et al. 2012). This paper reports the functional performance and the scientific feasibility of the NIRS3 instrument.

2 Scientific Objectives and Requirements

2.1 Spectral Analysis

The similarity in the albedos and reflectance spectra of C-type asteroids and carbonaceous chondrites (C chondrites) is compatible with the former, which may be the parent body of the latter (e.g. Johnson and Fanale 1973; Vilas and Gaffey 1989; Hiroi et al. 1996; Lantz et al. 2013). The abundant ratios of deuterium to hydrogen and that of $^{15}N/^{14}N$ of C chondrites present almost the same values as the Earth-Moon system (Saal et al. 2013), which supports the idea that C-type asteroids could be a candidate for the origin of terrestrial water as the remnants of icy planetesimals that delivered volatiles to the inner planets (Owen and Bar-Num 1995). To inspect the model of the water transportation inside the asteroids (Clayton and Mayeda 1999; Grimm and McSween 1989) and in the solar system (Owen and Bar-Num 1995), we should examine the scale of the variation of hydration and the dynamical history of the asteroids. Spectral observations over the surface including possible outcrops of the C-type asteroids in comparison with C chondrites can facilitate detecting and comprehending such events. However, the relationship between the spectral types of

C chondrites and those of C-type asteroids is still not so clear due to bias effects and space weathering. Telluric water absorption in the 3μm region also makes it difficult to detect hydroxide and hydrated mineral absorptions. The in-situ observations and sample return by Hayabusa2 will overcome these issues.

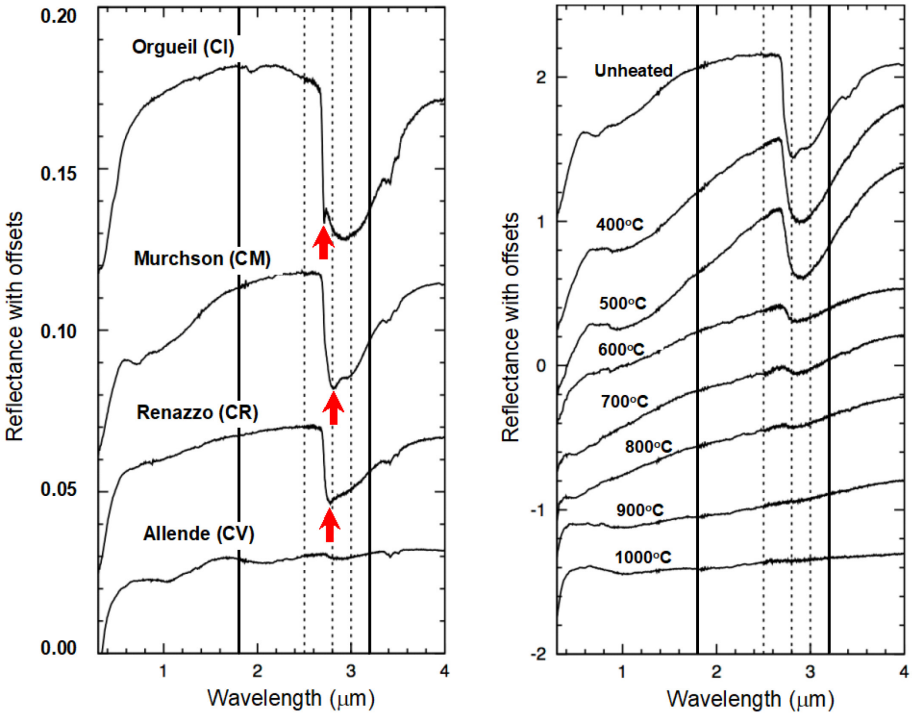

Fig. 1 Reflectance spectra of carbonaceous chondrites using the data from the NASA Reflectance Experiment Laboratory (RELAB). Left: Comparison of spectra among representative subgroups of C chondrites re-plotted after Hiroi et al. (1996). Red arrows indicate the features of hydroxide absorptions. Right: Comparison of spectra of CM chondrite Murchison with different thermal metamorphism re-plotted after Hiroi et al. (1996). Solid lines at 1.8 μm and 3.2 μm indicate the lower and upper limits of the NIRS3 spectral range, respectively. Dotted lines indicate the 2.5, 2.8 and 3μm wavelengths that are used to create the ratios for the scatterplot in Fig. 2.

C chondrites have been classified into subgroups according to their chemical composition, mineralogical organization, and oxygen-isotope ratio (e.g. Weisberg et al. 2006), each of which has characteristic reflectance spectra (e.g. Hiroi et al. 1996). The CM chondrites are considered to be the primitive solar system materials (McSween and Richardson 1977; Endress et al. 1996). CM chondrites, which are the most abundant subgroup, have a wide variation of aqueous alteration (McSween 1979; Browning et al. 1996). The wavelength position of the 3-μm absorption band reveals the degrees of aqueous alteration, which may be utilized to classify the subtypes of C chondrites (Takir at al. 2013). The absorption band depth should also reflect the stage of thermal metamorphism.

Figure 1 shows the comparisons for reflectance spectra of C chondrites using the data from the NASA Reflectance Experiment Laboratory (RELAB). Solid vertical lines at 1.8 and 3.2 μm indicate the lower and upper limits of the NIRS3 spectral range. The left figure compares the spectrum of each subgroup, such as CI, CM, CR, and CV, modified after Hiroi et al. (1996). The difference of the peak position, shape, and slope at wavelengths of 2.5 μm to 3.0 μm corresponds to the categories of subgroups.

To enable numerical analysis, we introduce a scatterplot of the reflectance spectra ratios (Figure 2). Dotted lines in Figure 1 indicate the 2.5, 2.8 and 3 μm wavelengths that are used to create the ratios for the scatterplot in Figure 2. Figure 2 (left) plots the ratio of spectral power at 2.8 to 2.5 μm and 3.0 to 2.5 μm for the samples of each subgroup of C chondrites. The black and red diagonal quadrangles depict the range of CM and CI chondrites that are plotted by black circles and red lozenges, respectively. Each range elongates from left bottom to right top.

Figure 1 (right) compares the spectra of the CM chondrite Murchison that was experimentally heated from room temperature to 1000°C for 1 week (after Hiroi et al. 1996). The decrease of the absorption depth of both hydroxide and hydrated minerals indicates the stage shift of thermal metamorphism that transcribes the highest temperature in the thermal history of the sample. Figure 2 (right) draws the scatterplot of the unheated to heated CM chondrite samples. Higher temperature moves the

plots to the top right direction as shown by a black arrow in the graph because the heating causes dehydration of phyllosilicates and reduction of 3 micron-band strength. This suggests that the elongated range of CM chondrites from left bottom to right top (Figure 2: left) may reflect the difference of thermal history after aqueous alteration. Red crosses in Figure 2 indicate the assumed errors of NIRS3 corresponding to a signal-to-noise ratio (SNR) of 50 at 2.6 μm. This demonstrates that the diagram can definitely distinguish the different degrees of dehydration observed in CM chondrites if the SNR exceeds 50.

The spectra of C-type asteroids have also been classified into sub-types by their spectral slope and the existence of absorption bands detected in ground observations (Bus et al. 2002; DeMeo et al. 2009). The effects of space weathering have been investigated by comparing spectra between ground observations up to 2.5 μm for some sub-types of asteroids and CM chondrites (Lantz et al. 2013). NIRS3 will obtain remote sensing data of Ryugu up to 3μm to analyze the similarity for the reflected spectra of C chondrites and, finally, those of returned samples. The results are expected to provide information about the status on the asteroid surface such as subgroup of C chondrites and the highest experienced temperature. We assess scientific requirements to determine corresponding C chondrites and temperature history of Ryugu in the next section.

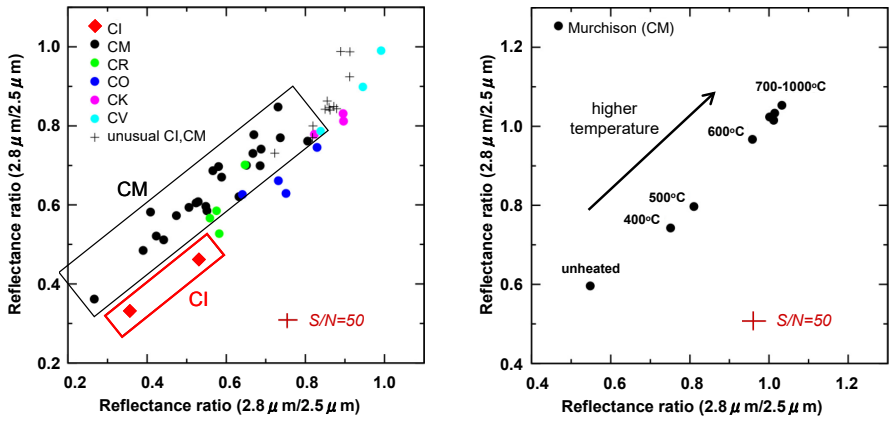

Fig. 2 Scatterplots of the reflectance spectra ratios at 2.5, 2.8, and 3.0 μm for the representative subgroup of carbonaceous chondrites (left) and CM chondrite Murchison with different thermal metamorphism (right). A red cross indicates the assumed errors of NIRS3 corresponding to a signal-to-noise ratio (SNR) of 50 at 2.6μm. Black and red diagonal quadrangles (left) cover the areas of CM and CI chondrites, respectively. A black arrow (right) presents the direction of dehydration by higher temperature.

2.2 Demand Specifications for the Instruments

NIRS3 aboard the Hayabusa2 spacecraft will primarily observe the asteroid in two modes of operation. The spacecraft basically stays in 'the home position' where the spacecraft altitude is 20 km, and all the instruments including NIRS3 perform global mapping utilizing the asteroid's rotation. Hayabusa2 will eventually shoot the asteroid creating an impact crater using the Small Carry-on Impactor (Arakawa et al. 2015; Saiki et al. 2015), hereafter, referred as the SCI crater. After the impact, the spacecraft will temporarily descend to an altitude of 1 km to observe the SCI crater, where alteration by space weathering is expected to be relatively weak, with higher spatial resolution. Considering these two phases of observation, we define the demand baseline specifications for NIRS3 as summarized in Table 1.

The longest spectral range for NIRS3 should be as long as 3.2 μm to cover the absorption band by the fundamental vibration O-H stretches and the overtone of the H_2O bend, which suggest the existence of hydroxide and hydrated minerals, at 2.7 to 3.0 μm. The longer wavelengths up to 3.6 μm can cover other absorption band by hydration and organic matters. It needs, however, newly developed sensors, such as mercury cadmium telluride (MCT), with active cooler, which does not fit in with the development schedule and mass budget of Hayabusa2. Thus, we decided to adopt 3.2 μm as the longest limit. The shortest wavelength is believed to have sufficient range of continuum spectra without absorption. Consequently, the spectral range of 1.8 to 3.2 μm also covers the primary absorption band of silicates (1.9 to 2.3 μm), phyllosilicates (1.9, 2.2-2.3, 2.7, and 2.9-3.2 μm) and carbonates (2.3, 2.5, and 2.8 μm).

Spectral sampling can almost be regarded as the resolution of wavelength, which is necessary to determine the peak wavelength, shape, and inclination of the absorption. The red arrows in Figure 1 (left) indicate the absorption features of hydroxide located

at 2.7-2.8 μm, which can be certainly detected by the wavelength resolution of 30 nm. Thus, we settled the resolution requirement to be less than 30 nm to distinguish the different degrees and stages in the sub-types of CM and CI chondrites. The measured value of the spectral sampling of NIRS3 sensor is 18 nm per pixel, which is better than requested as described in section 3.3.

The signal-to-noise ratio (SNR) is a function of the wavelength resolution and the accuracy of the output power of signals, which is directly related to the ability of NIRS3 to analyze spectroscopic data. In Figure 2, the red crosses indicate the resolution in the scatterplot with an SNR of 50 at 2.6 μm. The left figure indicates that an SNR of better than 50 can remarkably discriminate between CM and CI chondrites with different degrees of aqueous alteration. This value can provide estimated quantities of the hydrated minerals with accuracies of 2 wt % (weight percent), which can constrain the scale of the hydration variation on the asteroid. Figure 2 (right) also indicates that a SNR exceeding 50 allows evaluation of the highest temperatures that caused thermal metamorphism with a resolution of 100°C from room temperature to 700°C, which can constrain the dynamical history of the asteroid. Thus, we use an SNR of 50 at 2.6 μm to constrain the design of the observation system. The measured value was confirmed to be sufficient as described in section 4.4.

We defined the spatial sampling assuming SCI crater observations at 1 km altitude. The diameter of the crater is estimated as 10 m, at most, assuming that the surface is covered with sand where the micro-gravity affects the diameter, and to have a minimum of 1.4 m assuming that the surface is covered with rock (Arakawa et al. 2015). In the maximum case, the ejecta are expected to expand in a circular region with a radius of 25 m, assuming a depth of about 3 mm. In the minimum case, the ejecta are calculated to expand in a circular region with a radius of 3.5 m, assuming a depth of about 0.3 mm. Hence, a spatial resolution of 2 m is necessary to distinguish the spectra between the ejecta and non-ejecta materials. This spatial sampling corresponds to a field of view (FOV) of 0.11° at the NIRS3 optics, which provides spatial sampling of 40 m in global mapping at 20 km altitude. This spatial sampling at 20km is helpful to investigate surface spectral variations and space weathering processes.

The signal instability of the calibration lamps is required to examine the spatial variation of the hydration state in each observation area. It is, however, less strict than the SNR requirement because it does not affect on the shape of spectra. We settled the target value to be below 10%, which is measured as about 2%, as shown in section 4.5.

Table 1 Baseline specifications of NIRS3 from scientific objectives.

Parameter	Objective	Performance [1]	
		Required	Measured
Spectral range	- Absorption lines of hydroxide minerals and hydrated minerals - Continuum range without absorption	1.8 - 3.2 μm	1.8 - 3.2 μm
Spectral sampling	- Determining the positions and strength ratios of the absorption	< 30 nm	18 nm
Signal-to-noise ratio (SNR) [2]	- Determining the degree of aqueous alteration (CM or CI chondrite) and thermal metamorphism	> 50	> 300 (20 km) > 50 (1 km)
Spatial sampling	- Global mapping at 20 km - SCI crater observation at 1 km	< 40 m (20 km) < 2 m (1 km)	40 m (20 km) 2 m (1 km)
Signal instability	- Determining the absolute reflectance	< 10%	< 2%

[1] Numbers in parentheses indicate the observation altitudes. [2] SNR at 2.6 μm.

3 Instruments

3.1 Components and Interfaces

NIRS3 consists of the Spectrometric Unit (NIRS3-S), the Analog Electric Unit (NIRS3-AE), and the Harness Cables (NIRS3-HNS). Figure 3 presents a schematic block diagram of each component. Figures 4 and 5 present pictures of the FM of NIRS3-S and NIRS3-AE, respectively. NIRS3-S is installed on the -Z side on the -X panel of the Hayabusa2 spacecraft, and the aperture of optics is pointed toward the -Z in the spacecraft coordinate system. NIRS3-AE is installed on the back of the -X panel and is connected to NIRS3-S by NIRS3-HNS. Table 2 summarizes the fundamental interfaces and observation performance of NIRS3. The total mass of NIRS3 onboard components is 4.46 kg.

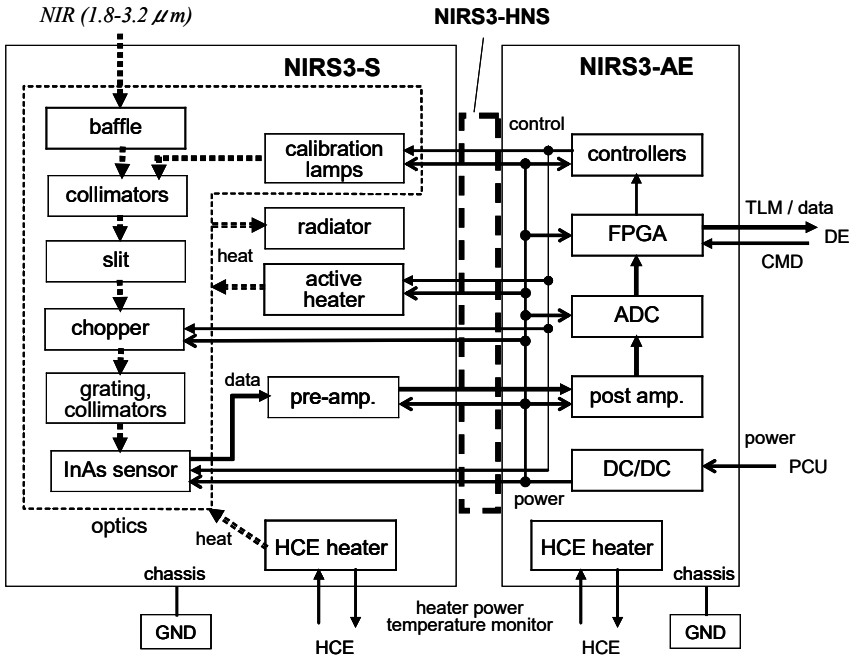

Fig. 3 Schematic block diagram of NIRS3 consisting of the Spectrometric Unit (NIRS3-S), the Analog Electric Unit (NIRS3-AE), and the Harness Cables (NIRS3-HNS). Abbreviations are denoted in the text.

Near-infrared light entering into the NIRS3-S aperture of optics is collimated, dispersed, and then detected by a linear-image sensor at the focal point. The detailed constitution and functions in the optics are described in the next section. The detected signals are amplified in the pre-amplifier (pre-amp), sent to NIRS3-AE through NIRS3-HNS, and amplified again in the post-amplifier (post-amp). The analog signals are then converted to digital data by the Analog-to-Digital Converter (ADC), and integrated and calculated by the Field-Programmable Gate Array (FPGA). The data reduced by the FPGA are acquired by the Digital Electronics (DE) of the spacecraft bus system on Hayabusa2 and down-linked to the ground stations.

A chopper with an electro-mechanically driven shutter is installed along the light path and switches the path between unmasked and masked. The sky-signals are detected when the path is open to the sky, and reference dark-signals are obtained when the path is masked by the shutter. The reference dark-signals are subtracted from the sky-signals at the FPGA, as described in the section 3.4 to remove the dark current and to reduce the electric drift effects in the data. Two small incandescent lamps are installed to supply standard light for intensity and wavelength calibration. The intensity calibration lamp (RAD; from radiation) has a constant voltage control mode with an input voltage of 5.0 V and constant current control mode with an input current of 165 mA and 85 mA. The wavelength calibration lamp (WAV), which is masked by a filter to display wavelength, is controlled by the constant voltage control mode with an input voltage of 5.0 V. The filter has two absorption peaks at 1.887 μm and 2.376 μm in the wavelength range of 1.8-3.2 μm. A radiator panel oriented toward the -X spacecraft axis radiates the heat of the optics, and an active heater at the optics controls the temperature there.

The FPGA in NIRS3-AE controls each function of the calibration lamps, the chopper, the active heater, and the sensor in NIRS3-S. FPGA sets the integration time of the detected voltage from 10 μs to 10 ms, and the stacking number accumulated by the sensor from 1 to 1024 (2^0 to 2^{10}), as shown in Table 2. The integration time is optimized at 10, 20, 40, 100, 200, 250, 400, and 600 μs, and 1, 1.2, 1.6, 1.8, 2, 2.5, 4, and 10 ms after the ground performance tests of the FM unit. The FPGA subtracts the reference dark-signal data from the sky-signal data formed by switching the chopper. There are three data sampling modes with different timing charts of the chopper, which are described in section 3.4 The FPGA also calculates the average, dispersion, maximum, and minimum values of the data for each spectral channel.

NIRS3 has telemetry, command, and mission data interfaces with the DE through the SpaceWire-based protocol. The data rate in the 256-stack nominal observation mode for global mapping is 2 kbps, and that in the 64-stack observation mode for the SCI crater is 8 kbps. The maximum data rate in the raw-data mode without subtraction and stacking is 500 kbps, which will be used only to diagnose the raw data

before data subtraction. The Power Control Unit (PCU) of the spacecraft bus system supplies electric power at voltages of 51.0 to 31.5 V to the NIRS3-AE direct-current to direct-current converter (DC/DC). The NIRS3-S and NIRS3-AE chassis are grounded to the spacecraft structure. The peak maximum electric power of NIRS3 onboard components is 14.9 W when the heater current is the maximum during observations. The nominal electric power is estimated as 9.9 W in the observation mode. Three sets of heaters with thermometers, which are powered and controlled by the Heater Control Electronics (HCE) of the bus system, are attached to each component (IRS3-AE, the pre-amp of NIRS3-S, and the optics of NIRS3-S) to maintain instrument survival temperature when the power of NIRS3 is turned off. The total maximum electric power of the HCE heater is distributed as 60 W.

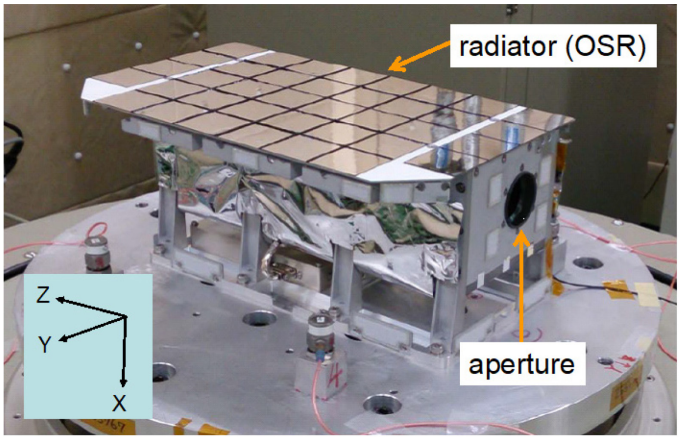

Fig. 4 NIRS3-S on the vibration test stage. MLI (multi-layer insulator) is not attached. A spacecraft coordinate system is indicated in a box.

Fig. 5 NIRS3-AE.

Table 2 Properties of NIRS3 instruments and observations.

Item	Value
Fundamental interfaces	
Total mass [1]	4.46 kg
Component mass	0.6 kg (AE), 3.58 kg (S), 0.28 kg (HNS)
Power	14.9 W (peak maximum) 9.9 W (nominal observation)
Bus voltage	+51.0 to +31.5 V
Data rate	2 kbps (nominal), 500 kbps (maximum)
Observation performances	
Spectral range	1.8-3.2 μm
Spectral sampling	18 nm/pixel
Field of view (FOV)	0.11° × 0.11°
Spatial resolution at one-shot [2]	40 m/spectrum at 20 km in altitude 2 m/spectrum at 1 km in altitude
Quantum bits	16 bit
Integration time	10, 20, 40, 100, 200, 250, 400, and 600 μs, 1, 1.2, 1.6, 1.8, 2, 2.5, 4, and 10 ms
Stacking number	2^n ; n = 0 to 10
Electric noise	< 3 mV_{rms}
Signal-to-noise ratio (SNR) at 2.6 μm [2]	> 300 at 20 km > 50 at 1 km

[1] The total mass of NIR3-S, NIRS3-AE, and NIRS3-HNS.
[2] Altitude above the asteroid surface.

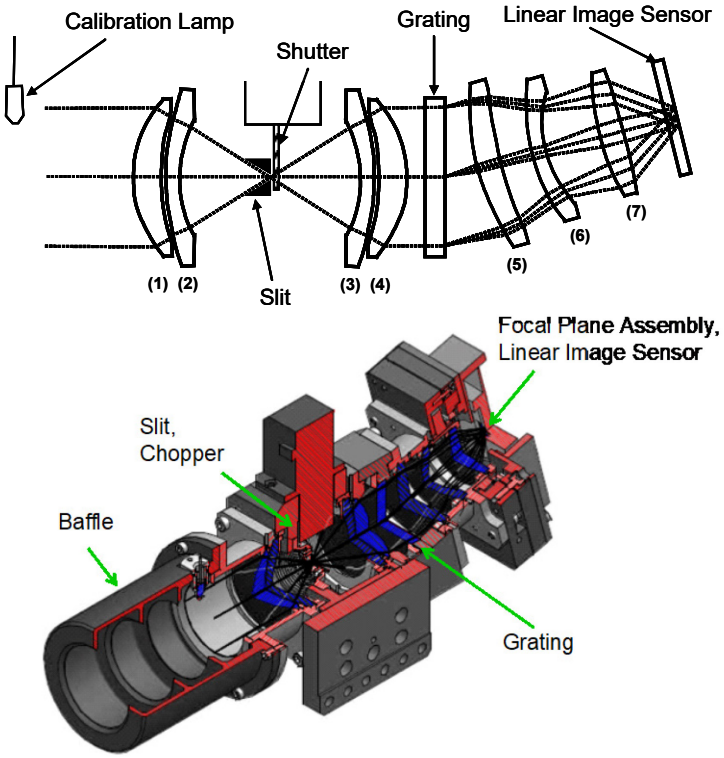

Fig. 6 Schematic diagram of the light path (above) and a cross section (below) of NIRS3-S optics. Numbers (1) to (7) denote the first to seventh SiGe lenses.

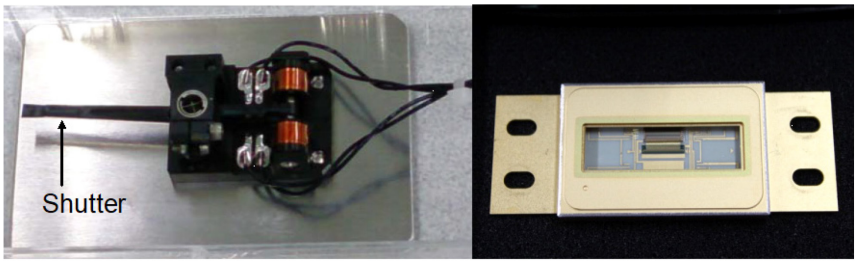

Fig. 7 NIRS3-S chopper (left) and the InAs image sensor (right).

3.2 Optics Design

NIRS3-S optics consist of a baffle; an objective; seven silicon-germanium (SiGe) lenses for collimating and focusing; a slit; a chopper; a flat transmission grating for dispersing; and the focal plane assembly (FPA) where a linear image sensor is installed. Table 3 indicates the optics characteristics and performance, and Figure 6 presents a schematic diagram of the light path and a cross section of optics. Pictures of the chopper and the linear-image sensor are shown in Figure 7. The aperture diameter measures 32 mm, and the 55 μm × 55 μm slit corresponds to a field of view (FOV) of 0.11°. This FOV performs spatial sampling of 40 m per shot at 20 km altitude in the home position observation phase. It also provides spatial sampling of 2 m in the observation phase of the SCI crater from the lower altitude at 1 km. Optics temperature is designed to be below 193 K (-80°C) at an altitude of 20 km to reduce the thermal noise and to simplify the cooling system as described in section 4.1. We adopted a chopper with an electromechanically driven shutter (Figure 7, left) considering durability and mass reduction. The chopper is placed behind the entrance slit and switches between sky-signal and reference dark-signal. The chopping frequency can be adjusted to about 100 Hz ±10% at 193 K, which regulates the readout frequency of the data to 100 Hz ±5%. The measured chopping frequency and data-acquiring interval are described in section 3.4.

Table 3 NIRS3 optics characteristics and performance.

Item	Value
Optical assembly	
Aperture diameter	32 mm
Collimator	seven SiGe lenses
F number	1.0
Slit size	55 μm × 55 μm
Spectrometer	grating
Optical transmission	0.6 - 0.9
Temperature [1]	< 188 K (-85°C) at 20 km [2]
	< 203 K (-70°C) at 1 km [2]
Chopper	
Shutter	electro-mechanical driven
Chopping frequency	95.9 Hz (at -80°C) ~ 94.4 Hz (at +25°C)
Sensor	
Photo diode	InAs (indium arsenide)
Pixel number	128 ch (linear)
Pixel size	50 μm pitch × 100 μm height
Quantum efficiency	40%
Dark current	< 100 nA at -20°C
RMS noise voltage	< 1 mV_{rms} at -20°C

1 Temperature to control the HCE heater (section 4.1).
2 Altitude above the asteroid surface.

3.3 InAs Linear-Image Sensor

We adopted a newly developed linear image sensor (Figure 7, right) with indium arsenide (InAs) photodiodes with high sensitivity at 2 to 3 μm wavelengths and a cut-off wavelength of 3.2 μm. Pixel size is designed as 50-μm pitch by 100-μm height to reduce the leakage current and to provide spatial margin against alignment errors. The InAs sensor has pixels of 128 channels and spectral sampling of 18 nm per pixel, whereas the indium gallium arsenide (GaInAs) sensor of NIRS has pixels of 64 channels and spectral sampling of 23.6 nm / pixel (Abe et al. 2006). This spectral sampling has enough resolution to satisfy the scientific requirement of less than 30 nm. The pixel of 1-128 ch corresponds to 1.5-3.45 μm (Matsuura et al. 2016); however, NIRS3 has sensitivity at 1.8-3.2 μm because of the cut-off wavelength of the grating and the InAs photodiode at a temperature of around 193 K. The 20 times difference in condenser capacity, 0.5 pF and 10 pF, enables switching to high-gain or low-gain mode to accommodate relatively lower or higher input signals. We concluded by observing the asteroid in high-gain mode after the confirmation of the performances as described in sections 4.3 and 4.4.

The designed values of dark current and readout noise are 1.3×10^{10} e/s and 3000 e_{rms}, respectively. The ground performance tests using the engineering model (EM) of the InAs sensor indicated that dark current ID depends on the sensor temperature T [°C] as follows.

$$I_D = 3.93 \times 10^{-8} \times 1.04^T \text{ [A]}$$

Assuming the capacitance of integration to be 0.5 pF, the maximum integration time is calculated as 880 μs at a sensor temperature of 193 K. The dark current then corresponds to 1.7×10^{-9} A, which produces the shot noise of 1.2 mV_{rms}. The readout noise of 3.0 mV_{rms} is, therefore, dominant in the total noise estimated to be 3.2 mV_{rms}. This value limits the total electrical noise of all the instruments (except for the sensor) to less than 0.5 mV_{rms}. Considering the local variation of albedo, we assume an albedo of 0.05 to calculate the SNR, which is 30% smaller than the value by Müller et al. (2010). The SNR is calculated to be 50 by using Ryugu's surface temperature of 300 K (Müller et al. 2010) at the aphelion where the solar distance is 1.4 AU. Consequently, the designed temperatures at the optics and the sensor must be below 193 K at 20 km in altitude. Because the SNR of the FM sensor is better than that of EM, we finally achieved SNR of 50 better than at the optics and the sensor of 203 K as described in section 4.4.

3.4 Data sampling

The data of the linear-image sensor are acquired by synchronizing to the opening and closing of the light pass at the chopper as shown in the timing chart in Figure 8. The chopper frequency measures 95.9 Hz at the optics temperature of 193 K (-80°C), which corresponds to one cycle of the chopper motion of 10.4ms. The timing to start acquisition is set by the trigger signals generated from the chopper motion. The opening period is longer than the closing period, and there are transient periods when the light pass is partially closed, as shown in Figure 8. The adjusted opening period is 5.8ms, and the closing period is 3.4ms. If the integration time added by read out time is sufficiently shorter than the opening or closing period, we can acquire multiple times of data acquisition in one opening or closing period to improve the SNR. We introduced two modes of multiple sampling: (3:1) which acquires three sky data and one reference dark-data, and (4:2) which acquires four sky data and two reference dark-data. The reference dark-signal data is subtracted from the sky-signal data in each sampling mode as in the following equation by denoting the first to fourth sky-signal data as S_1 to S_4 and the first to second reference dark-signal data as R_1 to R_2.

$$[\textit{Subtracted Data}\ (1{:}1)] = S_1 - R_1$$

$$[\textit{Subtracted Data}\ (3{:}1)] = [\, S_1 + S_2 + S_3 \,] / 3 - R_1$$

$$[\textit{Subtracted Data}\ (4{:}2)] = [\, S_1 + S_2 + S_3 + S_3] / 4 - [\, R_1 + R_2 \,] / 2$$

Assuming random noise, the SNR is 1.224 times better than in the single sampling mode of (1:1) due to the (3:1) mode, and 1.633 times better than the single sampling mode of (1:1) due to the (4:2) mode. The integration time of less than 600 μm and 250 μm can achieve (3:1) and (4:2) mode, respectively. In the chopper-off mode, the trigger signals for data acquisition are generated by FPGA, and the integration time can be extended up to 10 ms. Table 4 summarizes the observation modes and the assortment of the integration time in each observation mode.

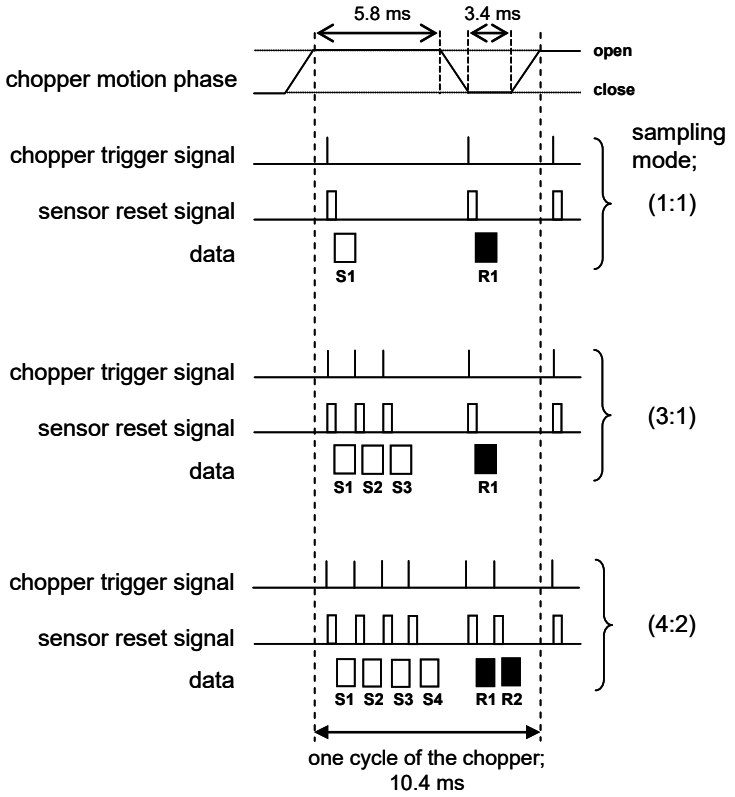

Fig. 8 Timing charts of the chopper motion and data acquisition by the multiple sampling mode of (1:1), (3:1), and (4:2) during one chopper cycle. S1 to S4 denote the first to the fourth sky-signal data, and R1 to R2 denote the first to the second reference dark-signal data.

Table 4 Observation modes versus chopper status, trigger signals, and multiple sampling. The integration times are denoted by x's.

Chopper status	off	on	on	on
Trigger signal	FPGA	chopper	chopper	chopper
Sampling (S:R)	N/A	(1:1)	(3:1)	(4:2)
Integration time				
10 μs	x	x	x	x
20 μs	x	x	x	x
40 μs	x	x	x	x
100 μs	x	x	x	x
200 μs	x	x	x	x
250 μs	x	x	x	x
400 μs	x	x	x	-
600 μs	x	x	x	-
1 ms	x	x	-	-
1.2 ms	x	x	-	-
1.6 ms	x	x	-	-
1.8 ms	x	x	-	-
2 ms	x	x	-	-
2.5 ms	x	x	-	-
4 ms	x	-	-	-
10 ms	x	-	-	-

4 Performance Confirmed by Ground Tests

4.1 Thermal Conditions for Optics

We have designed the temperature of the optics as 193 K (-80°C) considering the scientific requirements mentioned in section 3.3. Here, we describe the practical temperature obtained in the ground tests. We incorporated a passive radiator with optical solar reflectors (OSR) to cool down the optical and sensor assemblies below 193 K without using an active cooler. We conducted a trade-off study of the cooling mechanism after following the results of the thermal equilibrium tests using the EM of NIRS3 at Meisei Electric Co., Ltd., Isesaki, Japan, in November 2011. Consequently, we adopted an enlarged radiator with an OSR size of 0.0528 m^2 rather than attaching a Peltier thermoelectric device at the sensor due to its insufficiency of performance at

the temperature below 213 K (-60°C). We then reconstructed the thermal mathematical model for NIRS3-S and performed a thermal analysis using the thermal and optical properties, as indicated in Table 5. The revised model was confirmed in the second thermal equilibrium test in June 2012 after the radiator of EM was expanded.

Table 6 presents analyzed and operation temperatures at each part of NIRS3-S. Temperatures at the pre-amp, the optics, and the sensor are the results of the analysis using the thermal mathematical model, which is reconstructed after the thermal vacuum tests. They are at the observation phase of the home position (HP) at 20 km and low altitude (LA) at 1 km. The thermal analysis predicts that the temperature at the pre-amp in the thermal-dependent zone will be controlled to be 292 K (19°C). The temperatures at the optics and the sensor, in the thermal independent zone, will be 179 K (-94°C) and 193 K (-80°C) in the HP and LA phase, respectively.

Values in the column of the heater in Table 6 show the heater control temperatures for thermal stability at the optics and the sensor. We optimized them by considering the ambiguities of 5 K in the thermal analysis, which are 9 to 10 K higher than the analyzed temperatures. They are 188 K (-85°C) in the HP phase and 203 K (-70°C) in the LA phase. We use the results as settled operation temperatures in the following ground tests and evaluations. These on-orbit practical control temperatures can be revised after the checkout of the spacecraft after the launch,

Table 5 Thermal and optical properties for Thermal Analysis of NIRS3-S.

Item	Value
Solar radiation	1482 W m^{-2}
Asteroid Ryugu	
Shape, size	spherical, D = 1352 km
Properties	α = 1.0, ε = 0.9
Surface of NIRS3	
OSR	α = 0.2, ε = 0.84
MLI	α = 0.5, ε = 0.65
Thermal output	
Pre-amp	0.16 W
Sensor	0.09 W
Chopper	0.013 W

Notes- D : diameter, α : absorptance, ε : reflectance

Table 6 Analyzed and operation temperature at the parts of NIRS3-S.

phase	h	Temperature [K]			
	[km]	Pre-amp [1]	Optics [1]	Sensor [1]	Heater [2]
HP	20	292	179	179	188 (-85°C)
LA	1	292	193	193	203 (-70°C)

Notes- h : altitude, HP: Home position operation, LA: Low altitude operation.
[1] Temperatures calculated by the thermal analysis.
[2] Temperatures for the heater control to stabilize the temperatures at the optics and sensor.

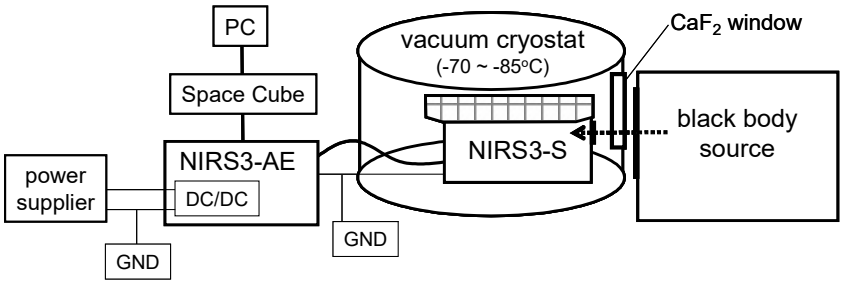

Fig. 9 Schematic diagram of the NIRS3 ground-performance tests and intensity-calibration tests using infrared radiation from a blackbody source.

4.2 Noise Measurements

We conducted ground performance tests to confirm the function and properties of NIRS3 systems such as response for signals, dark current, root-mean-square (RMS) noise, intensity calibration, and wavelength calibration. In this paper, we evaluate the noise, signal properties, and signal-to-noise ratio (SNR) derived from the ground-tests data. NIRS3 calibrations will be reported in Matsuura et al. (2016).

The main parts of the tests using the NIRS3 EM were conducted in September to December 2012, and the tests using the FM were conducted before and after environmental tests in July and November 2013. Figure 9 presents a schematic diagram of the ground-performance tests and intensity-calibration tests. Infrared rays from a blackbody source (Cavity blackbody source: CS1250-100, Electro Optical Industries) are emitted into NIRS3-S in a vacuum cryostat at Meisei Electric Co., Ltd., Isesaki, Japan. The optics temperature was adjusted between 213 K (-60°C) and 183 K (-90°C), which covers the HP and LA phase temperatures. Light from a halogen lamp was emitted into NIRS3-S through a monochromator during frequency-calibration tests. NIRS3-AE controls the inner calibration lamps, the chopper, and data acquisition at the sensor in NIRS3-S. NIRS3-AE is connected to a PC through Space Cube®, which is a SpaceWire-based computer simulating the data handling unit and the mission data processor of Hayabusa2. The chassis of both NIRS3-S and NIRS3-AE are grounded at one point to simulate the stability of electric currency in the configuration on the spacecraft.

Figure 10 (left) compares NIRS3's spectra of dark output voltage, and Figure 10 (right) plots dark output voltage to RMS noise for each pixel corresponding to the left figure. These data were obtained at the optics temperatures of 203 K (-70°C), 193 K (-80°C), and 188 K (-85°C). Temperatures of 203 K and 188 K simulate the observations at an altitude of 1 km for the SCI crater observations and 20 km for global mapping. The integration time is from 600 μs to 10 ms for 203 K and 193 K tests, and that for 188 K is from 1.0 to 2.5 ms as shown by the colors in each explanatory note box. The case of the integration time and the number of the data at 188K is fewer than those of 203 K and 193 K because we changed the optimized on-orbit practical control temperature at HP phase from 193 K to 188 K after the performance tests. However, the data are enough to evaluate the performance improvement from 193 K to 188 K because the noise at 188 K is as small as that at 193 K and the signal mainly depends on the maximum integration time as described later in this section. All the stack numbers are 1024.

The raw data of the InAs sensor output is expressed as count numbers: J [dn: data number] that are converted to voltages: V [V] by the following equation.

$$V_{out} = 5 / (1.5 \times 2^{16}) \times J \text{ [V]} = (5.086 \times 10^{-5}) \times J \text{ [V]}$$

The comparisons of the spectra at the different temperatures demonstrate that cooling the optics from 203 K to 193 K clearly reduces the dark current at each pixel and the dispersions between pixels. Data collected with different integration times suggest that the output is almost proportional to each integration time when it is relatively short; however, the voltages rapidly increase if the dark output exceeds 1 V. These results imply that it is important to adjust the integration time at each temperature to keep the dark output as below 1 V. Thus, we determined the maximum integration time as 2.5 ms at 188 K, 2.0 ms at 193 K, and 1.0 ms at 203 K.

Figure 11 compares spectra of the ratio of standard deviation at each pixel obtained in multiple-sampling modes (3:1) and (4:2) to that in the single-sampling mode (1:1). All the data are detected in 250-μs integration and 4096 stacks at optics temperatures of 193 K. The average ratio of the improvement in (3:1) mode is 1.227 ±0.010, which is consistent with the calculated value of 1.224 described in section 3.4. The value in the (4:2) mode is 1.623 ±0.013, which is also consistent with the predicted value of 1.633. These results indicate that the multiple-sampling mode effectively improves the SNR for relatively short integrated data.

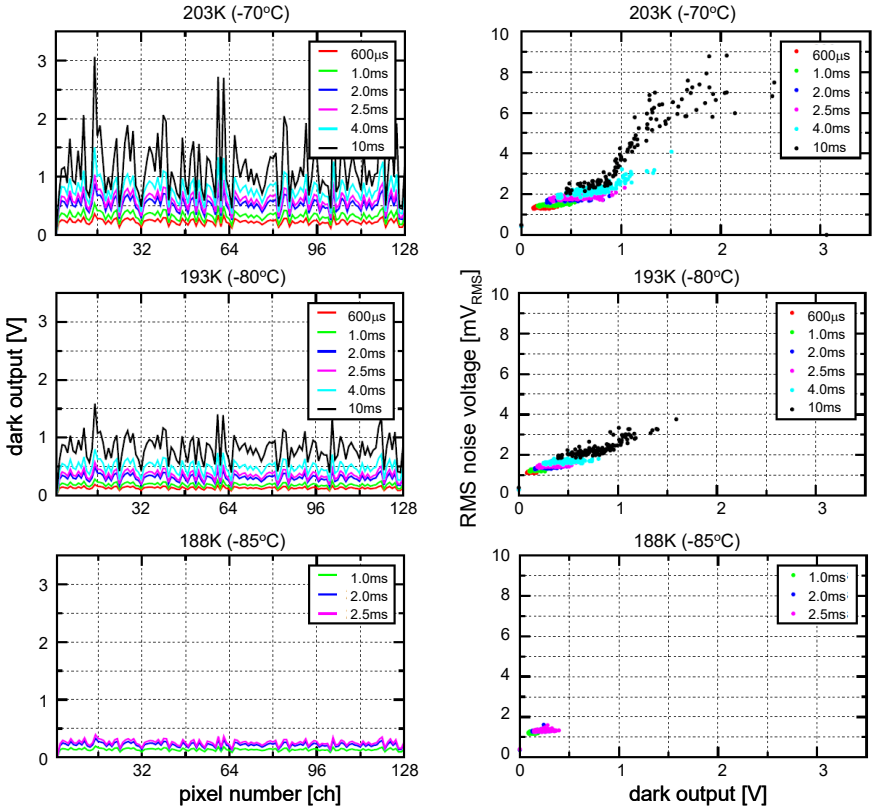

Fig. 10 Spectra of NIRS3 dark output voltage (left) and plots of dark output voltage to root-mean-square (RMS) noise (right). Data were obtained at sensor temperatures of 203 K (-70°C), 193 K (-80°C), and 188 K (-85°C). Colors of lines and plots indicate the integration time in each explanatory note. All the data are stacked by 1024.

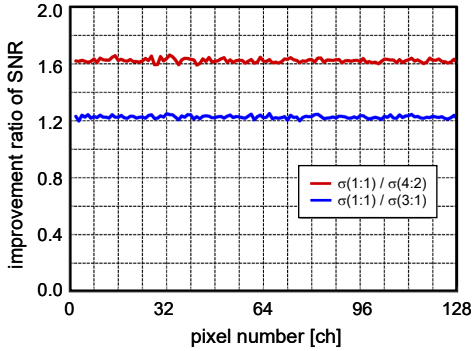

Fig. 11 Spectra of the ratio of standard deviation at each pixel obtained by the multiple sampling modes to the single-sampling mode using data of 250-μs integration and 4096 stacks, which shows the improvement of SNR.

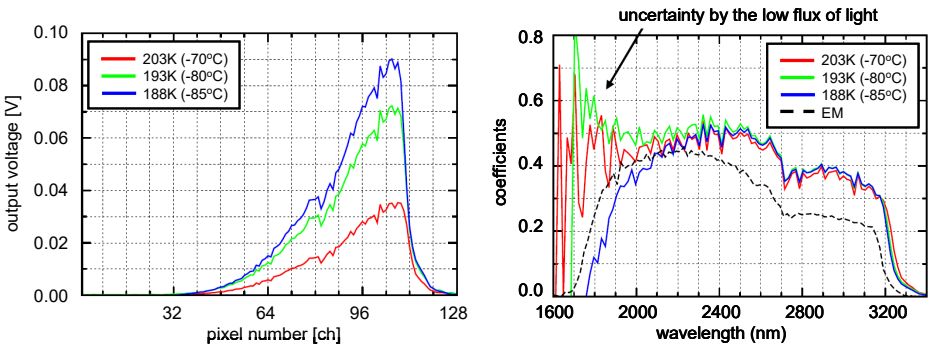

Fig. 12 Left: Spectra of blackbody radiation at 125°C with the parameters of NIRS3 optics temperature. Each integration time is described in the text. Right: Spectral response coefficients of NIRS3 system obtained from the spectra of the blackbody radiation. Colors of lines indicate the temperatures of optics as shown in the explanatory note boxes. The spectral response coefficient of the NIRS3 EM is plotted with a dashed line for comparison.

4.3 Signals Performances

We designed the spectral response coefficient of optics, the efficiencies of optical throughput which is the ratio of output power divided by input power at each wavelength, to be above 0.2 from 1.8 to 3.2 μm to achieve a sufficient SNR. We measured the coefficient by using the output signals of the blackbody sources. The radiation temperatures of the blackbody are switched to 125, 200, 250, 300, and 400°C to cover the minimum and maximum signal range of the reflection of Ryugu at wavelengths of 1.8 to 3.2 μm. In this paper, we deal with the case of 125°C to prove that NIRS3 has enough performance for the minimum intensity on orbit. Comparison of the output using different blackbody temperatures to investigate the linearity between input and output signals will be presented by Matsuura et al. (2016).

Figure 12 (left) presents examples of the blackbody radiation spectra at 125°C obtained at optics temperatures of 203 K (-70°C), 193 K (-80°C), and 188 K (-85°C). The integration time at 203 K is 1.0 ms, at 193 K is 2.0 ms, and at 188 K is 2.5 ms, which corresponds to the maximum integration time as determined in section 4.2. The input power at 3.2 μm almost conforms to the minimum case of asteroidal reflection. The increase of the output voltage at lower temperatures implies the remarkable improvement of the sensitivity to signals induced by cooling. The peak output voltages in Figure 12 (left) are 0.025 V, 0.072 V, 0.090 V at 203 K (-70°C), 193 K (-80°C), and 188 K (-85°C), respectively. The result shows that the signal at 193 K is 2.9 times higher and that at 188 K is 3.6 times higher than that at 203 K, which is mainly caused by longer integration time at the cooler temperature.

Figure 12 (right) displays the spectral response coefficients of NIRS3 system obtained from the spectra of the blackbody radiation. We used the equation obtained by Matsuura et al. (2016) to convert pixel number to wavelength. Values shorter than 2 μm have irregularities caused by the relatively low fluxes. The results indicate that the coefficients satisfy the requested value of more than 0.2 at wavelengths of 1.8 to 3.2 μm. The improvement of the coefficients from the EM to the FM can be seen at 2.6 to 3.2 μm; e.g. the FM coefficient of 0.47 at 2.6 μm is about 40% higher than the EM coefficient of 0.34. This is caused by the synergy of the technical improvement of the gain of InAs sensor and the adjustment of optics. Comparison of the spectra indicates that the output voltage for the signal slightly depends on the temperatures of optics due to complex effects induced by the sensitivity of InAs photo diodes, the characteristics of grating, and the deformation of optics that is adjusted at 193 K. The increase of the total sensitivity due to the lower temperature is about 0.8%/K from188 K to 193 K.

4.4 Evaluations of SNR On-orbit

The SNR is one of the most basic NIRS3 parameters for analyzing the aqueous alteration and the stage of thermal metamorphism as described in section 2.2. We estimate the on-orbit SNR by using the ground-test results and orbital plan for the scheduled period when Hayabusa2 stays at Ryugu from July 2018 to January 2020. We take account of the noise amplitude at each optics temperature and integration time shown in the plot of RMS noise (Figure 10, right). We calculate the intensity from the Ryugu surface at 2.6 μm with the assumed albedo of 0.05 as in the section 3.3. The estimated thermal radiation is also combined with the reflected intensity. We adopted the maximum integration time in section 4.2 and the spectral response coefficients at 2.6 μm in section 4.3. To derive the SNR in the lowest case, we presume that the angle of the observing point is 30° from the sub-earth point, the asteroidal surface is in the line from the Earth to the spacecraft, and the aging deterioration of the instrumental performances is 10%. Table 7 summarizes the observation parameters in each observation phase, which involves the observation altitude, maximum integration time, approximate sampling interval, nominal stack number, dark output, and RMS noise.

The lower graph in Figure 13 shows the results of the analyzed SNR history at 2.6 μm onboard the spacecraft during its stay at Ryugu. SNR values with and without thermal radiation are indicated as in the explanatory notes for the home-position (HP) operation and the low-altitude (LA) operation. The results indicate that the SNR at a wavelength of 2.6 μm exceeds 300 after 2.5 ms integration and 256-stacking at the home-position of 20 km in altitude for global mapping, which exceeds the requested value of more than 50. The average SNR after 1-ms integration and 64-stacking for the low-altitude operation of 1 km for SCI crater observations is lower than that in the previous case; however, it also exceeds 50 during the mission period.

Table 7 Observation parameters at each observation phase.

phase	h [km]	temperature at optics	$\Delta\tau$ [ms]	ΔT [s]	n	V_{dark} [V]	V_{rms} [mV]
HP	20	188 K (-85°C)	2.5	2.8	256	0.7	1.9
LA	1	203 K (-70°C)	1.0	0.7	64	0.8	2.0

HP: Home-position operation. LA: Low-altitude operation.
h: altitude, $\Delta\tau$: maximum integration time, ΔT: approximate sampling interval,
n: nominal stack number, V_{dark}: dark output, V_{rms} : RMS noise.

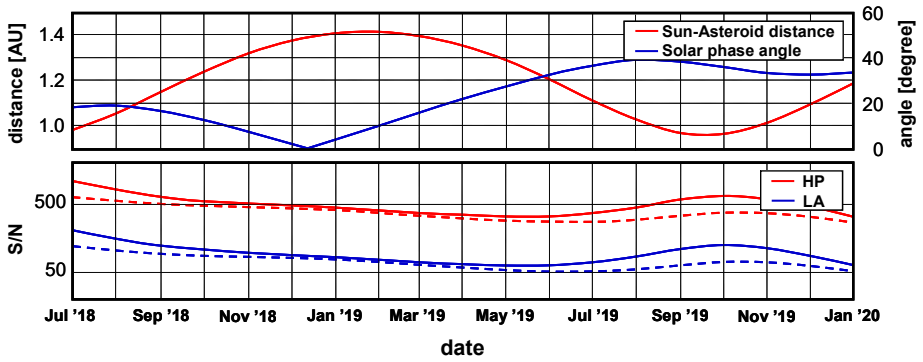

Fig. 13 Predicted history of heliocentric range, solar phase angle, and signal-to-noise ratio (SNR) of NIRS3 data at 2.6 μm during the home-position observations period at Ryugu. SNR with thermal radiation are indicated by solid lines, and those without thermal radiation are indicated by dashed lines. Correspondence between SNR and operation phases is denoted by the color shown in the explanation note, in which the abbreviations are the same as in Table 7.

4.5 Analysis of Calibration Lamps Stability

We investigated the calibration lamp stability by using the intensity calibration data obtained by the observations of calibration lamps RAD and WAV once every hour to several hours during the performance tests on November 10-14, 2014. Every measurement is made in typically one minute to avoid temperature instability by the heat of lamps. Results of the output voltage, current, and temperature are summarized in Table 8 with standard deviations of 1σ. Figure 14 shows the averaged spectra of calibration lamps RAD and WAV during the ground performance tests and calibration tests. The spectrum of WAV presents two absorption peak of about 50% in transmittance by the filter at 36 and 63 ch (blue arrows in Figure 14), which correspond to 1.887 μm and 2.376 μm, respectively. It has been confirmed that these peak positions do not shift in the temperature range of 183 to 213 K (Matsuura et al. 2016).

The deviation of temperature at each measurement by 1.1 K induces an output voltage deviation of 0.9% assuming the sensitivity dependence of 0.8%/K (section 4.3). The measured deviations of 1.4 to 1.8% are marginally larger than the temperature effect of 0.9%, suggesting other drift factors. The values are sufficiently below the instability requirement of less than 10%. However, it is recommended to monitor the intensity calibration every several days, because the Hayabusa2 mission period from the launch to the remote sensing observation is much longer than the test period of five days.

Table 8 Calibration lamps RAD and WAV characteristics.

Lamp	Input voltage [V]	Peak output voltage Average [mV]	Peak output voltage 1σ [%]	Current [mA]	Temperature [1] [K]	Control
RAD	5.0	40.08 ±0.71	1.8	75.0 ±0.4	191.8 ±1.1	constant voltage
	3.4	17.80 ±0.25	1.4	60.0 ±0.4	191.8 ±1.1	constant current [2]
WAV	5.0	34.02 ±0.61	1.8	71.9 ±0.4	191.8 ±1.1	constant voltage

[1] Output voltage at 51 ch. [2] Temperature at the InAs sensor. [3] Input current of 165 mA.

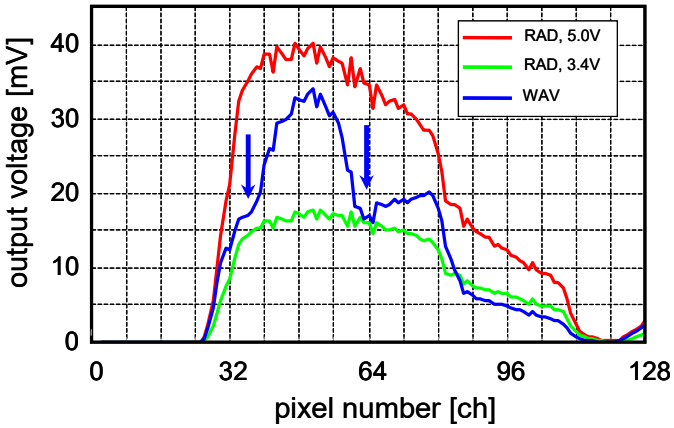

Fig. 14 Averaged spectra of calibration lamps RAD (input voltages of 5.0 V and 3.4 V), and WAV during ground-performance tests and calibration tests. Blue arrows at 36 and 63 ch indicate the absorption peak of the filter in WAV.

5 Conclusion

NIRS3 has been developed as a near-infrared spectrometer on Hayabusa2 spacecraft with a linear-image sensor to detect the absorption of hydrated and hydroxide minerals on the surface of the C-type asteroid Ryugu. It aims to examine the degrees of aqueous alteration, and the stage of thermal metamorphism which suggests the highest temperature on the asteroid surface. These scientific objectives require a spectral range of 1.8 to 3.2 μm, a spectral sampling of 30 nm/pixel, a signal-to-noise ratio (SNR) of > 50 at 2.6 μm, a field of view of 0.11° × 0.11°, and signal instability of < 10%. These properties have been confirmed to be sufficient after the environmental tests. The spectral sampling measures 18 nm/pixel. The predicted on-orbit SNR is calculated as more than 300, which far exceeds the scientific requirement. The signal instability measures < 2%, however, it is recommended to monitor the intensity calibration lamp every several days because the on-orbit mission period is much longer than the test period. These results prove that NIRS3 has sufficient performance to clarify the scale of the variation of hydration and the dynamical history of the asteroid.

Acknowledgments The authors are grateful to members of Meisei Electric Co., Ltd., particularly to Dr. Hajime Murao, Ms. Yuko Minagawa-Sakata, and Mr. Koji Taguchi for the design and development of the NIRS3 system and for supporting the ground-performance tests; to Dr. Norihide Takeyama (Genesia Corporation) for designing and adjusting the optical assembly; and to Mr. Sumura (Hamamatsu Photonics K.K.) for developing the InAs linear-image sensor. The authors are also thankful to Prof. Toshifumi Mukai, Prof. Hiroshi Murakami, Dr. Munetaka Ueno, and Mr. Hiroyuki Minamino (Japan Aerospace Exploration Agency) who provided many useful comments and advice especially for reducing noise and improving the optical performance of the NIRS3 system.

References

M. Abe, Y. Takagi, K. Kitazato, S. Abe, T. Hiroi, F. Vilas, B. E. Clark, P. A. Abell, S. M. Lederer, K. S. Jarvis, T. Nimura, Y. Ueda, and A. Fujiwara, Near-Infrared Spectral Results of Asteroid Itokawa from the Hayabusa Spacecraft, *Science*, **312**, 1334-1338, doi: 10.1126/science.1125718 (2006).

M. Arakawa, T. Saiki, K. Wada, T. Kadono, Y. Takagi, K. Shirai, C. Okamoto, H. Yano, M. Hayakawa, S. Nakazawa, N. Hirata, M. Kobayashi, P. Michel, M. Jutzi, H. Imamura, K. Ogawa, N. Sakatani, Y. Iijima, R. Honda, K. Ishibashi, H. Hayakawa, and H. Sawada, Science objective of Small Carry-on Impactor (SCI) and Deployable Camera 3 Digital (DCAM3-D): Observation of an ejecta curtain and a crater formed on the surface of 1999JU3 by an artificial high-velocity impact, *Space Sci. Rev.*, this issue (2016).

J-P. Bibring, C. Pilorget, C. Evesque. and V. Hamm, MicrOmega: an hyperspectral NIR microscope on board Hayabusa2, In *Abstract Asteroids, Comets, Meteors 2012*, #6399, Niigata, Japan (2012).

R. P. Binzel, A. W. Harris, S. J. Bus, T. H. Burbine, Spectral Properties of Near-Earth Objects: Palomar and IRTF Results for 48 Objects Including Spacecraft Targets (9969) Braille and (10302) 1989 ML, *Icarus*, **151**, 139-149 (2001).

L. B. Browning, H. Y. McSween Jr, M. E. Zolensky, Michael, Correlated alteration effects in CM carbonaceous chondrites, *Geochim. Cosmochim. Acta*, **60**, 2621-2633, doi: 10.1016/0016-7037(96)00121-4 (1996).

S. J. Bus, F. Vilas, and M. A. Barucci, Visible-Wavelength Spectroscopy of Asteroids, In *Asteroids III*, pp.169-182 (2002).

H. Campins, J. de León, A. Morbidelli, J. Licandro, J. Gayon-Markt, M. Delbo, and P. Michel,

The Origin of Asteroid 162173 (1999 JU3), *Astron. J.*, **146**, Issue 2, article id. 26, 6 pp., doi: 10.1088/0004-6256/146/2/26 (2013).

R. N. Clayton, and T. K. Mayeda, Oxygen isotope studies of carbonaceous chondrites., *Geochim. Cosmochim. Acta*, **63**, 2089–2104 (1999).

F. E. DeMeo, R. P. Binzel, S. M. Slivan, and S. J. Bus, An Extension of the Bus Asteroid Taxonomy into the Near-Infrared, *Icarus*, **202**, 160-180, doi: 10.1016/j.icarus.2009.02.005 (2009).

M. Endress, E. Zinner, and A. Bischoff, Early aqueous activity on primitive meteorite parent bodies, *Nature*, **379**, 701 – 703, doi:10.1038/379701a0 (1996).

R. E. Grimm and H. Y. Jr. McSween, Water and the thermal evolution of carbonaceous chondrite parent bodies. *Icarus*, **82**, 244–280 (1989).

T. Hiroi, M. E. Zolensky, C. M. Pieters, and M. E. Lipschutz, Thermal Metamorphism of the C, G, B, and F Asteroids: Seen from the 0.7 μm, 3 μm, and UV Absorption Strengths in Comparison with Carbonaceous Chondrites, *Meteor. Planet. Sci.*, **31**, 321-327, doi: 10.1111/j.1945-5100.1996.tb02068.x (1996).

T. V. Johnson andF. P. Fanale, Optical properties of carbonaceous chondrites and their relationship to asteroids, *J. Geophys. Res* , **78**, 8507-8518 (1973).

C. Lantz, B. E. Clark, M. A. Barucci, and D. S. Lauretta, Evidence for the effects of space weathering spectral signatures on low albedo asteroids, *Astron. & Astrophys*. **554**, A138, DOI: 10.1051/0004-6361/201321593 (2013).

D. Lazzaro, M. A. Barucci, D. Perna, F. L. Jasmim, M. Yoshikawa, and J. M. F. Carvano, Rotational spectra of (162173) 1999 JU3, the target of the Hayabusa2 mission, *Astron. & Astrophys.*, **549**, L2, DOI: 10.1051/0004-6361/201220629 (2013).

H. Y. McSween Jr., Are carbonaceous chondrites primitive or processed - A review, *Rev. Geophys. Space Phys.*, **17**, 1059-1078, doi: 10.1029/RG017i005p01059 (1979).

H. Y. McSween Jr. and S. M. Richardson, The composition of carbonaceous chondrite matrix, *Geochim. Cosmochim*. Acta, **41**, 1145-1161, doi:10.1016/0016-7037(77)90110-7 (1977).

T. G. Müller, J. Ďurech, S. Hasegawa, M. Abe, K. Kawakami, T. Kasuga, D. Kinoshita, D. Kuroda, S. Urakawa, S. Okumura, Y. Sarugaku, S. Miyasaka, Y. Takagi, P. R. Weissman, Y.-J. Choi, S. Larson, K. Yanagisawa, and S. Nagayama, Thermo-physical properties of 162173 (1999 JU3), a potential flyby and rendezvous target for interplanetary missions, *Astron. & Astrophys.*, **525**, A145, DOI: 10.1051/0004-6361/201015599 (2010).

S. Matsuura, K. Tsumura, K. Kitazato, T. Iwata, T. Senshu, *et al*., in preparation (2016).

T. Nakamura, T. Iwata, K. Kitasato, M. Abe, T. Osawa, M. Matsuoka, Y. Nakauchi, Y., T. Arai, M. Komatsu, T. Hiroi, N. Imae, A. Yamaguchi, and H. Kojima, Reflectance Spectra Measurement of Various Carbonaceous Chondrites using Hayabusa-2 Near Infrared Spectrometer, In *Abstract Annual meeting of the Meteoritical Society* (2015).

T. Owen and A. Bar-Nun, Comets, impacts, and atmospheres, *Icarus*, **116**, 215-226 (1995).

A. E. Saal, E. H. Hauri, J. A. Van Orman, and M. J. Rutherford, Hydrogen isotopes in lunar volcanic glasses and melt inclusions reveal a carbonaceous chondrites heritage, *Science*, **340**, 1317-1320 (2013).

T. Saiki, H. Imamura, M. Arakawa, K. Wada, Y. Takagi, M. Hayakawa, K. Shirai, H. Yano, and C. Okamoto, Small Carry-on Impactor (SCI) for Hayabusa2 Impact Experiment, *Space Sci. Rev*., this issue (2015).

D. Takir, J. P. Emery, H. Y. McSween Jr., C. A. Hibbitts, R. N. Clark, N. Pearson, A. Wang, Nature and degree of aqueous alteration in CM and CI carbonaceous chondrites, *Meterit. Planet. Sci*. **48**, 1618-1637 (2013).

F. Vilas, Spectral Characteristics of Hayabusa 2 Near-Earth Asteroid Targets 162173 1999JU3 and 2001 QC34, *Astron. J.*, **135**, 1101-1105, 10.1088/0004-6256/135/4/1101 (2008).

F. Vilas and M. J. Gaffey, Phyllosilicate absorption features in main-belt and outer-belt asteroid reflectance spectra, *Science*, **246**, 790-792 (1989).

M. K. Weisberg, T. J. McCoy, and A. N. Krot, Systematics and Evaluation of Meteorite Classification, In *Meteorites & the Early Solar System II*, pp.19-52 (2006).